NANO LETTERS

pubs.acs.org/NanoLett

Letter

Near-Atomic-Scale Mapping of Electronic Phases in Rare Earth Nickelate Superlattices

Bernat Mundet,* Claribel Domínguez, Jennifer Fowlie, Marta Gibert, Jean-Marc Triscone, and Duncan T. L. Alexander

Cite This: *Nano Lett.* 2021, 21, 2436−2443

Read Online

ACCESS | Metrics & More | Article Recommendations | Supporting Information

ABSTRACT: Nanoscale mapping of the distinct electronic phases characterizing the metal−insulator transition displayed by most of the rare-earth nickelate compounds is fundamental for discovering the true nature of this transition and the possible couplings that are established at the interfaces of nickelate-based heterostructures. Here, we demonstrate that this can be accomplished by using scanning transmission electron microscopy in combination with electron energy-loss spectroscopy. By tracking how the O *K* and Ni *L* edge fine structures evolve across two different $NdNiO_3$/$SmNiO_3$ superlattices, displaying either one or two metal−insulator transitions depending on the individual layer thickness, we are able to determine the electronic state of each of the individual constituent materials. We further map the spatial configuration associated with their metallic/insulating regions, reaching unit cell spatial resolution. With this, we estimate the width of the metallic/insulating boundaries at the $NdNiO_3$/$SmNiO_3$ interfaces, which is measured to be on the order of four unit cells.

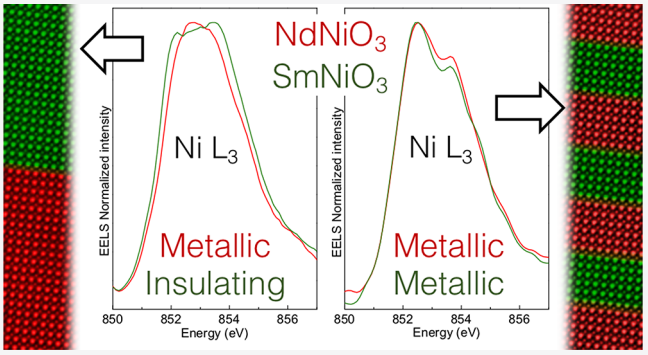

KEYWORDS: *STEM, EELS, nickelates, superlattices, phase mapping*

In order to fully understand the physics behind a particular phase transition, and to precisely control it for electronic devices, it is necessary to know how the characteristic phases emerge and evolve while crossing the transition. A paradigmatic case is the widely studied sharp metal−insulator transition (MIT) displayed by the rare-earth nickelate compounds (except $LaNiO_3$), which is strongly correlated to their structural properties.[1−9] In particular, this MIT is mainly regulated through the Ni−O−Ni bond angle and therefore it can be tailored by modifying the NiO_6 octahedral tilts characteristic of their distorted perovskite structure. This is typically accomplished either by changing the size of the rare earth cation[1,2,5] or by applying strain.[10−15] These compounds also exhibit a paramagnetic−antiferromagnetic phase transition at Néel temperatures (T_N) that either coincides with the MIT temperature (T_{MIT}) or is below it.[1,2] Even though this MIT is considered to be first order in all nickelates, presenting a clear hysteretic behavior and phase coexistence close to the T_{MIT},[16−18] the hysteretic behavior is significantly reduced in those compounds hosting a rare earth cation smaller than Nd, in which the magnetic order is suppressed at a lower temperature than the electronic one ($T_N < T_{MIT}$). In nickelate heterostructures, the MIT behavior might also be locally modulated. For instance, the presence of domain walls displaying signatures characteristic of a second order MIT was recently identified on the surface of $NdNiO_3$ thin films.[17] In addition to this finding, novel interfacial phenomena such as charge transfer or polar discontinuity effects might arise at coherent interfaces, as has been previously observed in some transition metal oxides[19,20] and even in some nickelate-based heterostructures,[12,21−28] which can also influence their electronic properties and hence their transitions. In order to investigate how such local phenomena influence the MIT, and to measure how distinct electronic phases behave at their interfaces, new characterization techniques capable of mapping phase coexistence at the atomic-scale level are required. To this end, various approaches have so far been used to map metallic and insulating phases in strongly correlated oxides: scanning tunneling microscopy;[29] near-field infrared microscopy;[17,30] scanning electron microscopy;[31] photoemission electron microscopy;[16] and conductive atomic force microscopy.[18] However, most of these techniques are mainly restricted to surface analysis and/or present a limited spatial resolution.

Received: November 16, 2020
Revised: January 29, 2021
Published: March 8, 2021

https://dx.doi.org/10.1021/acs.nanolett.0c04538
Nano Lett. 2021, 21, 2436−2443

In this work we demonstrate that aberration-corrected scanning transmission electron microscopy in combination with electron energy-loss spectroscopy (STEM-EELS) constitutes an alternative approach to identify and map metallic and insulating regions in rare-earth nickelate compounds. Compared to the aforementioned techniques, an atomic-resolution electron probe is used to scan the films under study and the transmitted electrons are collected by multiple detectors, each one providing complementary structural, chemical, and electronic information. STEM-EELS has already been demonstrated to be a powerful tool that can identify electronic state modulations occurring in specific lattice positions of transition metal oxide heterostructures.[32−37] For instance, this technique enabled the identification of local valence modulations occurring at the interfaces of $LaNiO_3$-based heterostructures induced by charge transfer effects.[26,38,39] In our study, however, since the Ni valence changes neither across the MIT nor from one nickelate compound to another, we also do not expect it to vary across the different electronic domains. Our approach is instead based on locally assessing electronic properties by looking at specific fingerprints, buried in the O *K* and Ni *L* edge fine structures, which are characteristic of the distinct electronic phases, as previously observed in X-ray absorption spectroscopy (XAS) experiments.[9,16,40−42] Here we demonstrate that this is possible, reaching around 3.5 Å spatial resolution.

As test samples for the experiment, we use two $[(NdNiO_3)_m/(SmNiO_3)_m]_L$ superlattices (SLs) grown epitaxially on (0 0 1)-oriented $LaAlO_3$ single crystal substrates by means of off-axis radiofrequency magnetron sputtering: a system that allows an "artificial" metallic−insulating phase separation to be engineered. One is a $(5,5)_{10}$ SL and the other a $(30,30)_2$, which respectively consist of either 5 or 30 pseudocubic unit cells per nickelate layer (m) and 10 or 2 periodic repetitions (L), giving an overall film thickness of around 35 nm in both cases. Figure 1a shows the X-ray diffraction $\theta-2\theta$ scans obtained from both SLs. The reflections and satellite peaks corresponding to each superlattice periodicity are observed, as well as finite-size oscillations, which confirm the epitaxial growth of the films and their high lattice quality. The transport properties of the films are measured using a van der Pauw configuration and are displayed in Figure 1b. The long period SL displays two MITs at ∼150 and ∼375 K, similar to those reported for single phase $NdNiO_3$ (100 K) and $SmNiO_3$ (380 K) thin films grown on $LaAlO_3$.[10,43,44] For the short period SL, however, a single MIT is identified at ∼200 K. The emergence of this singular electronic behavior, which was recently studied in a wider series of $NdNiO_3/SmNiO_3$ SLs, is ascribed to the energy cost associated with the metallic/insulating phase boundaries.[45] Accordingly, while keeping the experiment at room temperature, we can "artificially" modulate the electronic character associated with the $SmNiO_3$ layers. This is accomplished simply by lowering the SL periodicity, resulting in insulating or metallic behavior in the large or short period SL respectively. In contrast, the $NdNiO_3$ layers are metallic in both SLs at room temperature. We can therefore use these layers as a reference, as will be explained in more detail later.

The quality of the films was also evaluated by STEM-EELS. Atomic-scale imaging of the films was done by acquiring high-angle annular dark-field (HAADF) images of the two studied superlattices, which are displayed in Figure 2a). The obtained images demonstrate the high quality of the superlattice crystal,

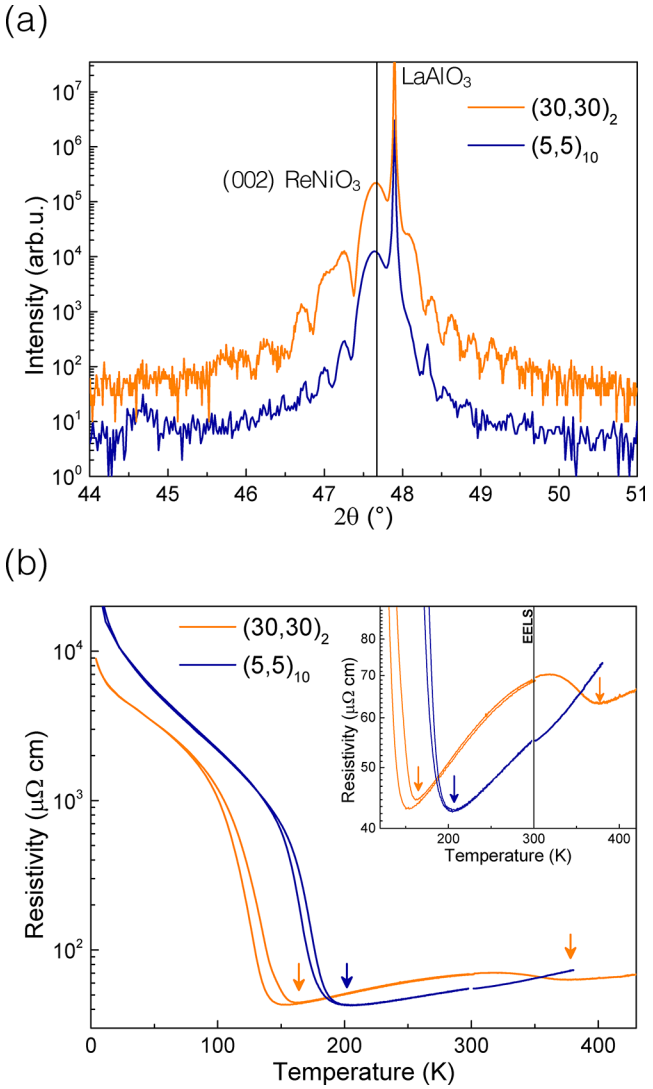

Figure 1. (a) X-ray diffraction $\theta-2\theta$ scans obtained from the $(5,5)_{10}$ (blue) and $(30,30)_2$ (orange) SLs. "Re" represents Nd or Sm. (b) Resistivity vs temperature curves measured in the $(5,5)_{10}$ (blue) and $(30,30)_2$ (orange) SLs using a van der Pauw configuration. Two MITs are identified (orange arrows) in the $(30,30)_2$ SL, whereas a single MIT (blue arrow) is identified in the $(5,5)_{10}$ SL. The inset shows an expanded view of the curves. The solid black line indicates the temperature at which the EELS experiments are carried out.

with coherent interfaces and without structural defects. Figure 2b) shows the Ni, Nd, and Sm EELS compositional maps obtained from a central region of the $(5,5)_{10}$ SL. The $NdNiO_3/SmNiO_3$ interfaces are observed to be atomically sharp, with a very low degree of atomic intermixing. Similar EELS compositional maps reveal the same interfacial quality in the other studied SL.[45]

We assess the electronic states of the films by evaluating the O *K* and Ni *L* edge fine structures. In this, we apply a concept established in XAS experiments,[40,42] but now using STEM-EELS to perform the measurements directly at the distinct layers of the films. Prior experiments in these SLs revealed that the films are sensitive to the incident electron beam flux, which can create significant amounts of oxygen vacancies while acquiring the EEL spectra. Careful testing finds that this degradation mainly depends on the pixel size, dwell time, and probe current used to acquire the EELS spectrum image (SI).

https://dx.doi.org/10.1021/acs.nanolett.0c04538
Nano Lett. 2021, 21, 2436−2443

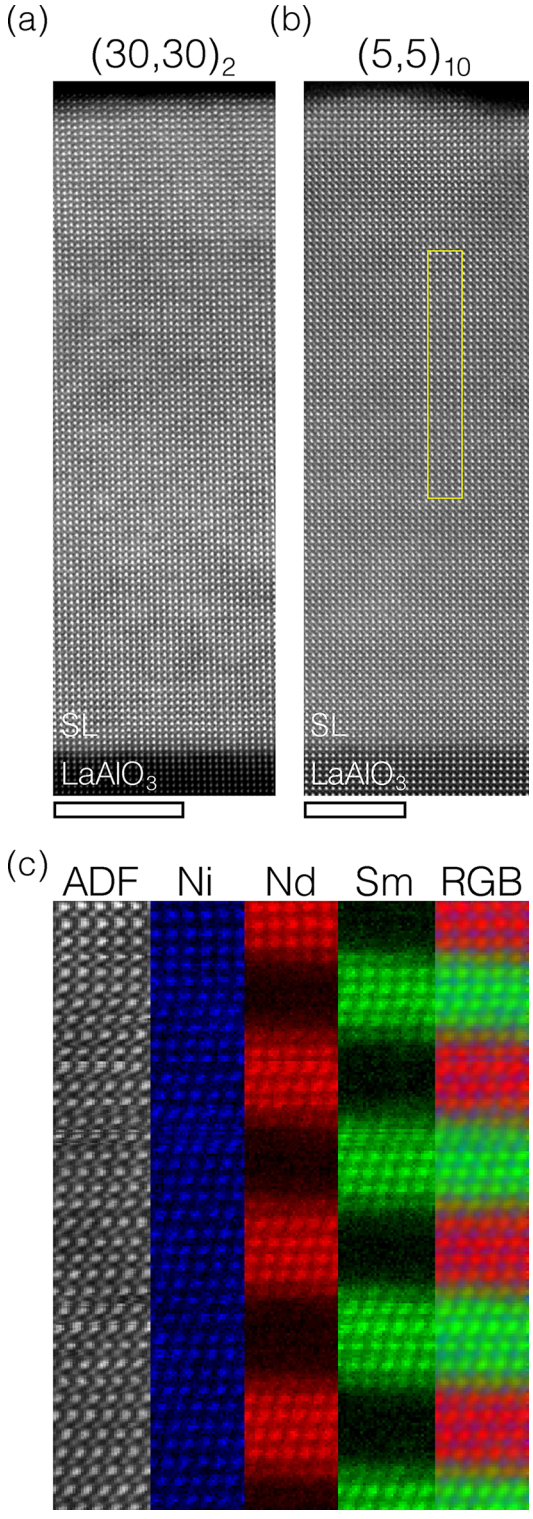

Figure 2. Atomic-resolution high-angle annular dark-field (HAADF) images of the (a) $(30,30)_2$ and (b) $(5,5)_{10}$ SLs. Scale bar: 10 nm. (c) EELS spectrum image data obtained from the area indicated by the yellow box in panel (b). From left to right: HAADF image, Ni (blue), Nd (red), and Sm (green) compositional maps, and RGB map where the three previous EELS maps are overlaid. The Ni, Nd, and Sm signals are extracted from the Ni *L*, Nd *M*, and Sm *M* edges, after spectral background subtraction.

Avoiding this degradation therefore limits the spatial resolution of the experiment. Specifically, by using a pixel size of around 3.5−4 Å, dwell times on the order of 0.1 s/pixel, and a probe current of around 80 pA, we were able to scan the same film area several times without inducing significant damage. With these conditions, we found that a 0.1 eV/channel energy dispersion gave a good compromise between spectral energy resolution and signal-to-noise ratio (SNR). Another critical aspect is that we improved the energy resolution by reducing the energy spread of the incident electron beam with the use of a monochromator, obtaining a zero-loss peak (ZLP) full width at half-maximum (FWHM) of ∼0.4 eV for the energy dispersion used to acquire the data. More discussion about the experimental parameters and trade-offs are presented in the Supporting Information.

With this approach, we recorded the O *K* edge spectra associated with either the $NdNiO_3$ (red) or $SmNiO_3$ (green) layers belonging to the $(30,30)_2$ and $(5,5)_{10}$ SLs shown in Figure 3a,b, respectively.

The displayed spectra are the integration of many pixel spectra specifically selected from the corresponding layers. In

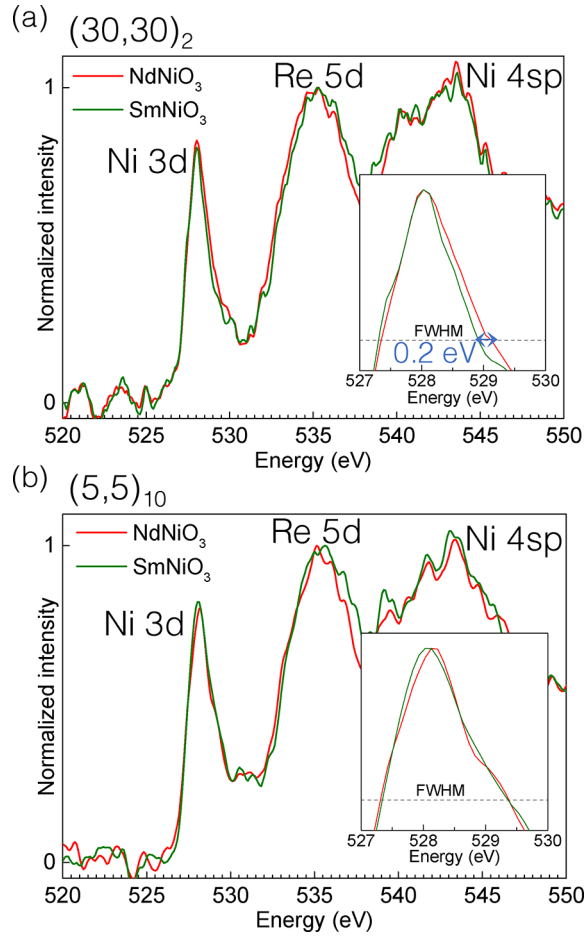

Figure 3. EEL spectra of the O *K* edge measured in the $NdNiO_3$ (red) and $SmNiO_3$ (green) layers of the (a) $(30,30)_2$ and (b) $(5,5)_{10}$ SLs. "Re" represents rare earth. Each spectrum is made by integrating several spectra obtained from distinct but analogous layers. The spectra have been slightly smoothed and normalized to the maximum intensity of the Re 5d peak to better appreciate the difference between the layers. A direct comparison between the raw and smoothed data is presented in the Supporting Information. The insets show an expanded view of the normalized O *K* prepeak. The dashed lines indicate the full width at half-maximum (FWHM) of the O *K* prepeak.

https://dx.doi.org/10.1021/acs.nanolett.0c04538
Nano Lett. 2021, 21, 2436−2443

this case, energy shift instabilities have been corrected by realigning each pixel spectrum according to the ZLP position, acquired near-simultaneously using a dual-EELS configuration (see Supporting Information). The O *K* edge gives us information about the electronic excitations from the O 1s core level to the empty O 2p electronic states. In rare-earth nickelate compounds, these O 2p states are hybridized with the Ni 3d, rare earth 5d, and Ni 4sp electronic states, giving rise to a first prepeak located at around 528 eV, followed by two main peaks located at 535 and 542 eV, respectively.[40,46] In order to compare the spectral variations between the distinct layers, we normalize all of the spectra to the maximum intensity of the main peak located at around 535 eV, after background subtraction. We focus our study on the O *K* edge prepeak, since it is very sensitive to subtle changes in the Ni−O bonds. For instance, its amplitude significantly decreases under oxygen removal.[46] Considering that no significant changes in the prepeak intensity are identified across either SL, the samples are judged to have uniform oxygen content distributions. In addition, the intensity of this prepeak is similar to those reported in previous works and therefore we can assume that our films are stoichiometric.[40,47] However, a more careful inspection of the prepeak shape measured in the $(30,30)_2$ SL allows us to identify a subtle drop in the prepeak area in the $SmNiO_3$ layers. This effect has been attributed to the Ni 3d bandwidth shrinking,[40,47] stemming from the lowering of the Ni 3d and O 2p orbital overlap when the Ni−O−Ni angle decreases. To better compare this effect with previous studies, we also normalize the O *K* spectra to their prepeak maximum (see insets), from which we extract their FWHM values. We observe that, in the $(30,30)_2$ SL, the prepeak is approximately 0.2 eV narrower in the $SmNiO_3$ layers than in the $NdNiO_3$ ones. Although this value is at the edge of the attainable energy resolution, it is in agreement with those values reported using XAS from either bulk crystals[40] or thin films.[42] Moreover, this broadening effect occurs in all $SmNiO_3$ layers of this SL, as shown in the Supporting Information. Looking instead at the prepeak fine structures obtained from the $(5,5)_{10}$ SL, we observe that both $SmNiO_3$ and $NdNiO_3$ layers present similar prepeak shapes, i.e., similar areas and widths, indicating that the degree of hybridization between the Ni 3d and O 2p bands is now similar across the whole SL. This is not surprising if we take into account that the prepeak also becomes around 0.2 eV broader when crossing the MIT from the insulating to the metallic state, as previously observed in $NdNiO_3$ and $PrNiO_3$ crystals.[40] Since the octahedral tilts do not significantly change in the $SmNiO_3$ layers when lowering the SL periodicity,[45] this broadening effect, occurring in the $(5,5)_{10}$ SL with respect to the $(30,30)_2$ SL, therefore derives from the fact that the $SmNiO_3$ layers are metallic in the former case. As such, this result constitutes the first direct observation of the metallic behavior of the $SmNiO_3$ layers at room temperature in the $(5,5)_{10}$ SL.

While the O *K* edge results give a first indication of the local electronic state measurements, the changes observed in this edge are subtle. Therefore, we turn our attention to possible modulations occurring in the Ni *L* edge fine structure at the distinct nickelate layers, which are expected to be more pronounced.[40] The Ni *L* edge fine structures obtained from the $(30,30)_2$ and $(5,5)_{10}$ SLs are displayed in Figure 4a,b, respectively. The displayed integrated spectra are normalized either to the Ni L_2 peak or Ni L_3 peak (insets) maximum intensity, after background subtraction and energy shift

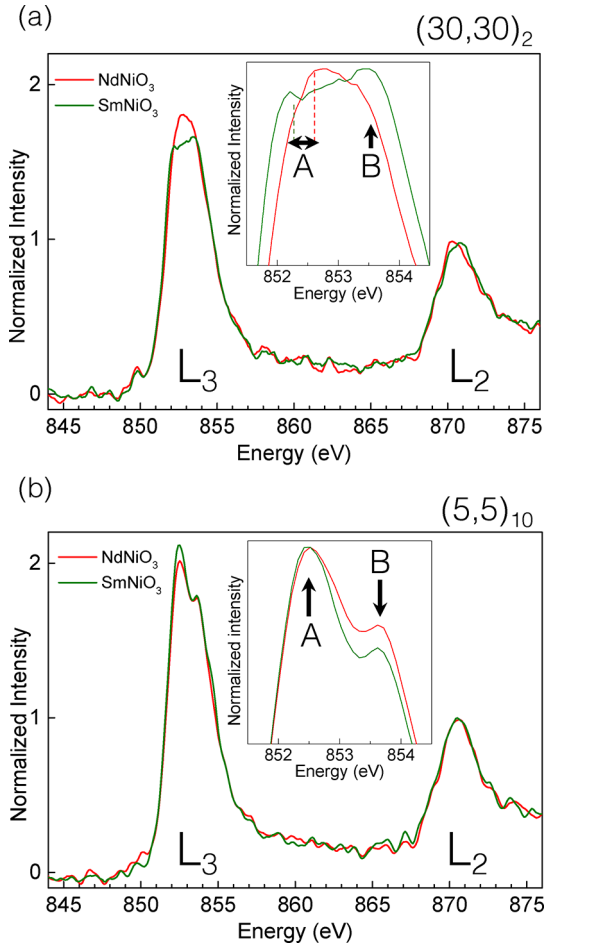

Figure 4. Ni *L* edge spectra obtained from the $NdNiO_3$ (red) and $SmNiO_3$ (green) layers of the (a) $(30,30)_2$ and (b) $(5,5)_{10}$ SLs normalized to the L_2 peak height. Each spectrum is made by integrating several spectra obtained from distinct but analogous layers. The spectra have been slightly smoothed to better appreciate the difference between the layers. A direct comparison between the raw and smoothed data is presented in the Supporting Information. The insets show an amplified view of the Ni L_3 peak, in this case normalized to the Ni L_3 peak. The Ni L_3 peak is composed of two secondary peaks that are labeled as peak A and peak B. The red and green dashed lines in panel (a) indicate the approximate position of peak A in the $NdNiO_3$ and $SmNiO_3$ layers, respectively.

calibration to the La *M* edge from the $LaAlO_3$ substrate. In order to further verify that the areas under study were not damaged during the specimen preparation, the O *K* edge fine structure was also assessed nearby. Because the Ni L_2 fine structure depends on the Ni valence,[48−50] the observed shape and the fact that it does not change across the SLs confirm that the Ni valence (close to nominal +3) is constant across both SLs and that neither charge transfer effects nor accumulation of oxygen vacancies occur at the layer interfaces. In agreement with other works, the Ni L_3 peak is composed of two secondary peaks located at approximately 852 and 854 eV, that we label as peak A and peak B, respectively.[9,16,40,42] These two peaks are more separated in energy in the insulating state, also having a more pronounced dip between them. Correlated to this larger splitting, peak A is slightly shifted toward lower energies (by a few hundreds of meV) in the insulating regions.[16] Even though the Ni L_3 fine structure depends on the nickelate compound, the change in the peak splitting is more significant

https://dx.doi.org/10.1021/acs.nanolett.0c04538
Nano Lett. 2021, 21, 2436−2443

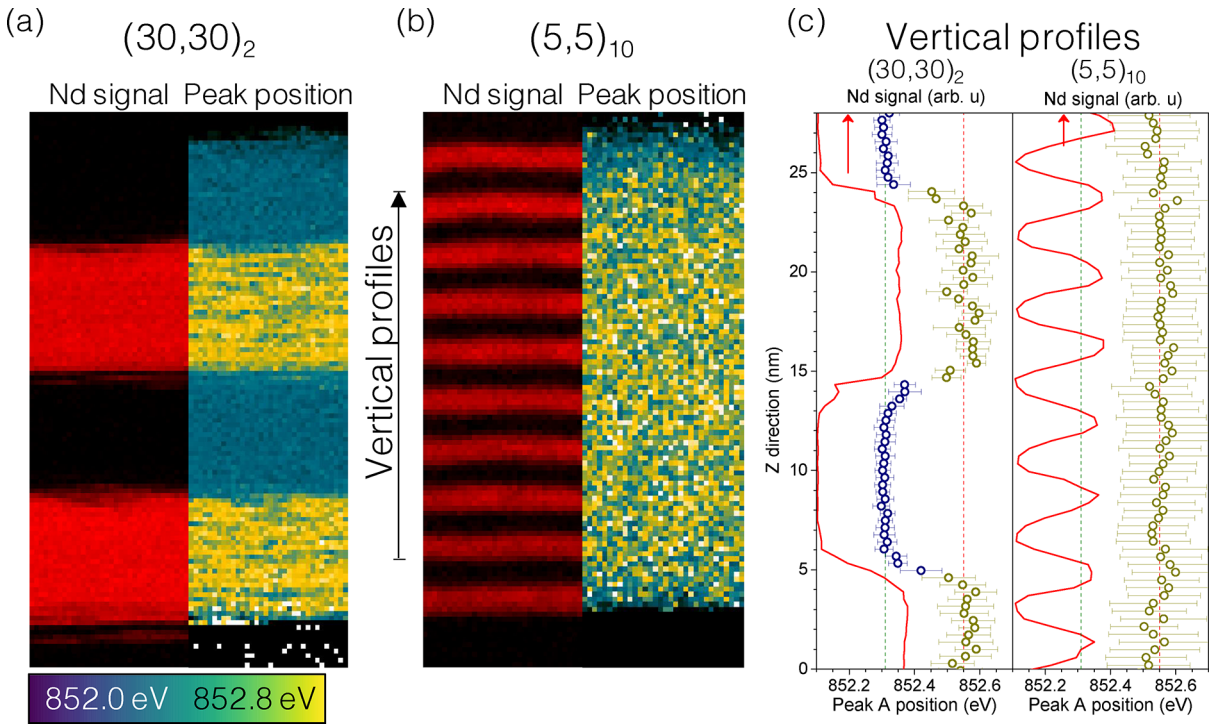

Figure 5. Nd compositional map (left panel) and peak A position map (right panel) obtained from the (a) $(30,30)_2$ and (b) $(5,5)_{10}$ SLs. (c) Depth profiles of the Nd content (red solid line) and peak A position (open symbols) calculated from the maps shown in panels (a) and (b). Each dot is the average of each row of pixels, and the error bars correspond to their standard deviation. The limits of the profiles are indicated with an arrow between panels (a) and (b). Two distinct peak positions are clearly identified in the $(30,30)_2$SL (green and red dashed lines), whereas one single value is observed in the profile obtained from the $(5,5)_{10}$SL (red dashed line).

when crossing the MIT rather than when changing the rare-earth cation size.[40] Accordingly, we can use this spectral signature to evaluate the electronic character associated with distinct nickelate regions.

We analyze first how the Ni L_3 peak evolves across the $(30,30)_2$ SL (see Figure 4a). In this SL each nickelate layer presents a distinct fine structure. In particular, peak A is shifted by around 0.2 eV toward lower energies in the $SmNiO_3$ layers, with increased splitting of the two secondary peaks, which agrees well with the fact that the $NdNiO_3$ layers are metallic and the $SmNiO_3$ layers are insulating in this SL. However, a different observation is made in the $(5,5)_{10}$ SL, the one displaying a single MIT, whose Ni L edges are shown in Figure 4b. In this case, both layers present similar Ni L edge fine structures, with both secondary peaks equally separated and fixed at the same spectral positions. This provides further evidence that the electronic state associated with the $SmNiO_3$ layers is different in the $(30,30)_2$ and $(5,5)_{10}$ SLs and that they are metallic, like the $NdNiO_3$ layers, in the short period SL.

Having established which spectral signatures are associated with each electronic phase, we now explore how they evolve across the superlattices. As previously mentioned, peak A shifts to lower energies in the insulating state. Therefore, we can use this fingerprint to track the evolution of the electronic character across the SLs. In order to map the position of peak A across the SLs, in each pixel spectrum of the SI the rise of the Ni L_3 peak is fitted to a Gaussian profile, and its associated central position is then extracted. Prior to the fitting procedure, a principal component analysis (PCA) algorithm is applied to the SI data in order to reduce random noise components. Since PCA filtering can introduce artifacts in the fine structure of core-loss edges,[51,52] we have limited its use to mapping purposes, where improved SNR is required for fitting each individual pixel spectrum. The width of the overall Ni L_3 peak was also assessed, in order to verify that the measured shifts are not associated with spectral energy shift instabilities, as shown in the Supporting Information. From the calculated peak A position values, we generate the color maps shown in the right panels of Figure 5a,b, for the $(30,30)_2$ and $(5,5)_{10}$SLs, respectively. These maps are plotted alongside their corresponding Nd compositional maps (left panels), as generated from the same data set, in order to compare peak position with layer type. To aid this comparison, the SNR is improved by integrating and averaging all of the peak positions/Nd signals contained in each pixel line, which are then represented as depth profiles in Figure 5c for both SLs.

As expected, two distinct positions for peak A are identified in the $(30,30)_{10}$ SL, associated with the different nickelate layers. In particular, peak A moves to lower energies (blue color) in the $SmNiO_3$ layers and to higher energies in the $NdNiO_3$ ones (yellow color), which agree well with our previous results. Given that the pixel size is of the order of one pseudocubic unit cell, the metallic/insulating phase boundaries are rather sharp, with an approximate width of four unit cells. This value agrees very well with the propagation length of the structural distortions observed at these interfaces.[45] On the contrary, no color-wise changes are identified across the $(5,5)_{10}$ SL map, with peak A always being located at the spectral position that is characteristic of the metallic state, further confirming that the whole SL is now metallic.

While these measurements are at the limit of what can currently be done with EELS spectrometer detection using conventional charge-coupled device cameras, our results demonstrate that they allow characterization of the electronic

https://dx.doi.org/10.1021/acs.nanolett.0c04538
Nano Lett. 2021, 21, 2436−2443

properties in local positions of nickelate heterostructures with about one pseudocubic unit cell spatial resolution. Given that the spatial resolution is mainly limited by the allowable beam flux, it should be possible to improve this by using newly commercially available direct electron detector cameras with the EELS spectrometer, which offer much better energy resolution and SNR resulting from the improved point spread function and detective quantum efficiency.[53,54] These improved properties should permit a finer spatial sampling of the spectral signal while maintaining the same allowable electron dose/flux, toward atomic-resolution measurements. We further expect that our approach will open a new experimental avenue associated with the investigation of electronic phase distributions in rare-earth nickelates. An example of this is to apply the methodology across a temperature range in order to map how the electronic phases evolve when crossing the metal−insulating transitions displayed by both superlattices.

In summary, we have shown that monochromated STEM-EELS can be used to map electronic phase coexistence in rare-earth nickelate compounds, providing at least unit cell spatial resolution. By evaluating the O *K* and Ni *L* edge fine structures, we demonstrate the local measurement of electronic state in two $NdNiO_3/SmNiO_3$ superlattices, having distinct periodic lengths, which display either one or two metal−insulator transitions. While, at room temperature, the $NdNiO_3$ layers are always metallic, the $SmNiO_3$ layers are insulating in the large period SL but metallic in the short period SL. By tracking how the Ni L_3 fine structure evolves across both SLs, we not only image the metallic/insulating regions in both cases, verifying the room temperature metallic nature of the $SmNiO_3$ layers in the short period SL, but also estimate the width of the metallic/insulating boundaries in the long period SL.

■ ASSOCIATED CONTENT

Supporting Information

The Supporting Information is available free of charge at https://pubs.acs.org/doi/10.1021/acs.nanolett.0c04538.

Additional STEM and EELS information (PDF)

■ AUTHOR INFORMATION

Corresponding Author

Bernat Mundet − *Department of Quantum Matter Physics, University of Geneva, 1211 Geneva, Switzerland; Electron Spectrometry and Microscopy Laboratory (LSME), Institute of Physics (IPHYS), École Polytechnique Fédérale de Lausanne (EPFL), 1015 Lausanne, Switzerland;* orcid.org/0000-0003-0608-2070; Email: bernat.mundetbolos@unige.ch, bernatmundet@gmail.com

Authors

Claribel Domínguez − *Department of Quantum Matter Physics, University of Geneva, 1211 Geneva, Switzerland*

Jennifer Fowlie − *Department of Quantum Matter Physics, University of Geneva, 1211 Geneva, Switzerland;* orcid.org/0000-0002-3528-6390

Marta Gibert − *Physik-Institut, University of Zurich, 8057 Zurich, Switzerland*

Jean-Marc Triscone − *Department of Quantum Matter Physics, University of Geneva, 1211 Geneva, Switzerland*

Duncan T. L. Alexander − *Electron Spectrometry and Microscopy Laboratory (LSME), Institute of Physics (IPHYS), École Polytechnique Fédérale de Lausanne (EPFL), 1015 Lausanne, Switzerland;* orcid.org/0000-0003-4350-8587

Complete contact information is available at: https://pubs.acs.org/10.1021/acs.nanolett.0c04538

Notes

The authors declare no competing financial interest.

■ ACKNOWLEDGMENTS

This work was partly supported by the Swiss National Science Foundation through Division II Grant No. 200020_179155. The research leading to these results received funding from the European Research Council under the European Union's Seventh Framework Program (FP7/2007-2013)/ERC Grant Agreement 319286 Q-MAC). M.G. acknowledges support by the Swiss National Science Foundation under Grant No. PP00P2_170564. We acknowledge access to the electron microscopy facilities at the Interdisciplinary Centre for Electron Microscopy (CIME), École Polytechnique Fédérale de Lausanne. B.M. and D.T.L.A. thank Dr. A. Teurtrie and Prof. C. Hébert for fruitful discussions.

■ ABBREVIATIONS

EELS, electron energy-loss spectroscopy; FWHM, full width at half-maximum; MIT, metal−insulator transition; SI, spectrum image; SL, superlattice; SNR, signal-to-noise ratio; STEM, scanning transmission electron microscopy; ZLP, zero-loss peak

■ REFERENCES

(1) Medarde, L. Structural, Magnetic and Electronic Properties of Perovskites (R = Rare Earth). *J. Phys.: Condens. Matter* **1997**, *9*, 1679−1707.

(2) Catalan, G. Progress in Perovskite Nickelate Research. *Phase Transitions* **2008**, *81* (7−8), 729−749.

(3) Mizokawa, T.; Khomskii, D.; Sawatzky, G. A. Spin and Charge Ordering in Self-Doped Mott Insulators. *Phys. Rev. B: Condens. Matter Mater. Phys.* **2000**, *61*, 11263.

(4) Varignon, J.; Grisolia, M. N.; Íñiguez, J.; Barthélémy, A.; Bibes, M. Complete Phase Diagram of Rare-Earth Nickelates from First-Principles. *npj Quantum Mater.* **2017**, *2*, 21.

(5) Torrance, J. B.; Lacorre, P.; Nazzal, A. I.; Ansaldo, E. J.; Niedermayer, C. Systematic Study of Insulator-Metal Transitions in Perovskites $RNiO_3$ (R = Pr,Nd,Sm,Eu) Due to Closing of Charge-Transfer Gap. *Phys. Rev. B: Condens. Matter Mater. Phys.* **1992**, *45* (14), 8209−8212.

(6) Mercy, A.; Bieder, J.; Íñiguez, J.; Ghosez, P. Structurally Triggered Metal-Insulator Transition in Rare-Earth Nickelates. *Nat. Commun.* **2017**, *8*, 1677.

(7) Park, H.; Millis, A. J.; Marianetti, C. A. Site-Selective Mott Transition in Rare-Earth-Element Nickelates. *Phys. Rev. Lett.* **2012**, *109*, 156402.

(8) Johnston, S.; Mukherjee, A.; Elfimov, I.; Berciu, M.; Sawatzky, G. A. Charge Disproportionation without Charge Transfer in the Rare-Earth-Element Nickelates as a Possible Mechanism for the Metal-Insulator Transition. *Phys. Rev. Lett.* **2014**, *112*, 106404.

(9) Bisogni, V.; Catalano, S.; Green, R. J.; Gibert, M.; Scherwitzl, R.; Huang, Y.; Strocov, V. N.; Zubko, P.; Balandeh, S.; Triscone, J. M.; Sawatzky, G.; Schmitt, T. Ground-State Oxygen Holes and the Metal-Insulator Transition in the Negative Charge-Transfer Rare-Earth Nickelates. *Nat. Commun.* **2016**, *7*, 1−8.

(10) Catalano, S.; Gibert, M.; Bisogni, V.; Peil, O. E.; He, F.; Sutarto, R.; Viret, M.; Zubko, P.; Scherwitzl, R.; Georges, A.; Sawatzky, G. A.; Schmitt, T.; Triscone, J. M. Electronic Transitions in Strained $SmNiO_3$ Thin Films. *APL Mater.* **2014**, *2* (11), 116110.
(11) Catalano, S.; Gibert, M.; Fowlie, J.; Iñiguez, J.; Triscone, J. M.; Kreisel, J. Rare-Earth Nickelates $RNiO_3$: Thin Films and Heterostructures. *Rep. Prog. Phys.* **2018**, *81* (4), 046501.
(12) Middey, S.; Chakhalian, J.; Mahadevan, P.; Freeland, J. W. W.; Millis, A. J. J.; Sarma, D. D. Physics of Ultrathin Films and Heterostructures of Rare Earth Nickelates. *Annu. Rev. Mater. Res.* **2016**, *46* (1), 305−314.
(13) Catalan, G.; Bowman, R. M.; Gregg, J. M. Metal-Insulator Transitions in $NdNiO_3$ Thin Films. *Phys. Rev. B: Condens. Matter Mater. Phys.* **2000**, *62* (12), 7892−7900.
(14) Liu, J.; Kargarian, M.; Kareev, M.; Gray, B.; Ryan, P. J.; Cruz, A.; Tahir, N.; Chuang, Y. De; Guo, J.; Rondinelli, J. M.; Freeland, J. W.; Fiete, G. A.; Chakhalian, J. Heterointerface Engineered Electronic and Magnetic Phases of $NdNiO_3$ Thin Films. *Nat. Commun.* **2013**, *4*, 2714.
(15) Xiang, P. H.; Zhong, N.; Duan, C. G.; Tang, X. D.; Hu, Z. G.; Yang, P. X.; Zhu, Z. Q.; Chu, J. H. Strain Controlled Metal-Insulator Transition in Epitaxial $NdNiO_3$ Thin Films. *J. Appl. Phys.* **2013**, *114* (24), 243713.
(16) Mattoni, G.; Zubko, P.; Maccherozzi, F.; Van Der Torren, A. J. H.; Boltje, D. B.; Hadjimichael, M.; Manca, N.; Catalano, S.; Gibert, M.; Liu, Y.; Aarts, J.; Triscone, J. M.; Dhesi, S. S.; Caviglia, A. D. Striped Nanoscale Phase Separation at the Metal-Insulator Transition of Heteroepitaxial Nickelates. *Nat. Commun.* **2016**, *7*, 13141.
(17) Post, K. W.; McLeod, A. S.; Hepting, M.; Bluschke, M.; Wang, Y.; Cristiani, G.; Logvenov, G.; Charnukha, A.; Ni, G. X.; Radhakrishnan, P.; Minola, M.; Pasupathy, A.; Boris, A. V.; Benckiser, E.; Dahmen, K. A.; Carlson, E. W.; Keimer, B.; Basov, D. N. Coexisting First- and Second-Order Electronic Phase Transitions in a Correlated Oxide. *Nat. Phys.* **2018**, *14*, 1056−1061.
(18) Preziosi, D.; Lopez-Mir, L.; Li, X.; Cornelissen, T.; Lee, J. H.; Trier, F.; Bouzehouane, K.; Valencia, S.; Gloter, A.; Barthélémy, A.; Bibes, M. Direct Mapping of Phase Separation across the Metal-Insulator Transition of $NdNiO_3$. *Nano Lett.* **2018**, *18* (4), 2226−2232.
(19) Zubko, P.; Gariglio, S.; Gabay, M.; Ghosez, P.; Triscone, J.-M. Interface Physics in Complex Oxide Heterostructures. *Annu. Rev. Condens. Matter Phys.* **2011**, *2* (1), 141−165.
(20) Hwang, H. Y.; Iwasa, Y.; Kawasaki, M.; Keimer, B.; Nagaosa, N.; Tokura, Y. Emergent Phenomena at Oxide Interfaces. *Nat. Mater.* **2012**, *11* (2), 103−113.
(21) Hoffman, J.; Tung, I. C.; Nelson-Cheeseman, B. B.; Liu, M.; Freeland, J. W.; Bhattacharya, A. Charge Transfer and Interfacial Magnetism in $(LaNiO_3)_n/(LaMnO_3)_2$ Superlattices. *Phys. Rev. B: Condens. Matter Mater. Phys.* **2013**, *88* (14), 1−7.
(22) Disa, A. S.; Walker, F. J.; Ismail-Beigi, S.; Ahn, C. H. Research Update: Orbital Polarization in $LaNiO_3$-Based Heterostructures. *APL Mater.* **2015**, *3*, 062303.
(23) Patel, R. K.; Meyers, D.; Liu, X.; Mandal, P.; Kareev, M.; Shafer, P.; Kim, J. W.; Ryan, P. J.; Middey, S.; Chakhalian, J. Emergent Behavior of $LaNiO_3$ in Short-Periodic Nickelate Superlattices. *APL Mater.* **2020**, *8*, 041113.
(24) Grutter, A. J.; Yang, H.; Kirby, B. J.; Fitzsimmons, M. R.; Aguiar, J. A.; Browning, N. D.; Jenkins, C. A.; Arenholz, E.; Mehta, V. V.; Alaan, U. S.; Suzuki, Y. Interfacial Ferromagnetism in $LaNiO_3$/$CaMnO_3$ Superlattices. *Phys. Rev. Lett.* **2013**, *111* (8), 1−5.
(25) Hepting, M.; Minola, M.; Frano, A.; Cristiani, G.; Logvenov, G.; Schierle, E.; Wu, M.; Bluschke, M.; Weschke, E.; Habermeier, H. U.; Benckiser, E.; Le Tacon, M.; Keimer, B. Tunable Charge and Spin Order in $PrNiO_3$ Thin Films and Superlattices. *Phys. Rev. Lett.* **2014**, *113* (22), 227206.
(26) Grisolia, M. N.; Varignon, J.; Sanchez-Santolino, G.; Arora, A.; Valencia, S.; Varela, M.; Abrudan, R.; Weschke, E.; Schierle, E.; Rault, J. E.; Rueff, J. P.; Barthélémy, A.; Santamaria, J.; Bibes, M. Hybridization-Controlled Charge Transfer and Induced Magnetism at Correlated Oxide Interfaces. *Nat. Phys.* **2016**, *12*, 484−492.
(27) Catalano, S.; Gibert, M.; Fowlie, J.; Iñiguez, J.; Triscone, J. M.; Kreisel, J. Rare-Earth Nickelates $RNiO_3$: Thin Films and Heterostructures. *Rep. Prog. Phys.* **2018**, *81* (4), 046501.
(28) Gibert, M.; Viret, M.; Zubko, P.; Jaouen, N.; Tonnerre, J. M.; Torres-Pardo, A.; Catalano, S.; Gloter, A.; Stéphan, O.; Triscone, J. M. Interlayer Coupling through a Dimensionality-Induced Magnetic State. *Nat. Commun.* **2016**, *7*, 1−7.
(29) Fäth, M.; Freisem, S.; Menovsky, A. A.; Tomioka, Y.; Aarts, J.; Mydosh, J. A. Spatially Inhomogeneous Metal-Insulator Transition in Doped Manganites. *Science* **1999**, *285* (5433), 1540−1542.
(30) Qazilbash, M. M.; Brehm, M.; Chae, B. G.; Ho, P. C.; Andreev, G. O.; Kim, B. J.; Yun, S. J.; Balatsky, A. V.; Maple, M. B.; Keilmann, F.; Kim, H. T.; Basov, D. N. Mott Transition in VO_2 Revealed by Infrared Spectroscopy and Nano-Imaging. *Science* **2007**, *318*, 1750.
(31) Kim, T. H.; Angst, M.; Hu, B.; Jin, R.; Zhang, X. G.; Wendelken, J. F.; Plummer, E. W.; Li, A. P. Imaging and Manipulation of the Competing Electronic Phases near the Mott Metal-Insulator Transition. *Proc. Natl. Acad. Sci. U. S. A.* **2010**, *107* (12), 5272−5275.
(32) Gauquelin, N.; Hawthorn, D. G.; Sawatzky, G. A.; Liang, R. X.; Bonn, D. A.; Hardy, W. N.; Botton, G. A. Atomic Scale Real-Space Mapping of Holes in $YBa_2Cu_3O_{6+\delta}$. *Nat. Commun.* **2014**, *5*, 4275.
(33) Gloter, A.; Tieri, G.; Li, D.; Caputo, M.; Strocov, V. N.; Stéphan, O.; Triscone, J. M.; Gariglio, S. Role of Point and Line Defects on the Electronic Structure of $LaAlO_3/SrTiO_3$ Interfaces. *APL Mater.* **2020**, *8*, 041103.
(34) Hartman, S. T.; Mundet, B.; Idrobo, J. C.; Obradors, X.; Puig, T.; Gázquez, J.; Mishra, R. Direct Observation of Apical Oxygen Vacancies in the High-Temperature Superconductor $YBa_2Cu_3O_{7-X}$. *Phys. Rev. Mater.* **2019**, *3*, 114806.
(35) Gazquez, J.; Luo, W.; Oxley, M. P.; Prange, M.; Torija, M. A.; Sharma, M.; Leighton, C.; Pantelides, S. T.; Pennycook, S. J.; Varela, M. Atomic-Resolution Imaging of Spin-State Superlattices in Nanopockets within Cobaltite Thin Films. *Nano Lett.* **2011**, *11* (3), 973−976.
(36) Gloter, A.; Badjeck, V.; Bocher, L.; Brun, N.; March, K.; Marinova, M.; Tencé, M.; Walls, M.; Zobelli, A.; Stéphan, O.; Colliex, C. Atomically Resolved Mapping of EELS Fine Structures. *Mater. Sci. Semicond. Process.* **2017**, *65*, 2−17.
(37) Gauquelin, N.; Benckiser, E.; Kinyanjui, M. K.; Wu, M.; Lu, Y.; Christiani, G.; Logvenov, G.; Habermeier, H. U.; Kaiser, U.; Keimer, B.; Botton, G. A. Atomically Resolved EELS Mapping of the Interfacial Structure of Epitaxially Strained $LaNiO_3/LaAlO_3$ Superlattices. *Phys. Rev. B: Condens. Matter Mater. Phys.* **2014**, *90* (19), 1−11.
(38) Gibert, M.; Viret, M.; Torres-Pardo, A.; Piamonteze, C.; Zubko, P.; Jaouen, N.; Tonnerre, J. M.; Mougin, A.; Fowlie, J.; Catalano, S.; Gloter, A.; Stéphan, O.; Triscone, J. M. Interfacial Control of Magnetic Properties at $LaMnO_3/LaNiO_3$ Interfaces. *Nano Lett.* **2015**, *15* (11), 7355−7361.
(39) Phillips, P. J.; Rui, X.; Georgescu, A. B.; Disa, A. S.; Longo, P.; Okunishi, E.; Walker, F.; Ahn, C. H.; Ismail-Beigi, S.; Klie, R. F. Experimental Verification of Orbital Engineering at the Atomic Scale: Charge Transfer and Symmetry Breaking in Nickelate Heterostructures. *Phys. Rev. B: Condens. Matter Mater. Phys.* **2017**, *95* (20), 1−8.
(40) Freeland, J. W.; Van Veenendaal, M.; Chakhalian, J. Evolution of Electronic Structure across the Rare-Earth $RNiO_3$ Series. *J. Electron Spectrosc. Relat. Phenom.* **2016**, *208*, 56−62.
(41) Piamonteze, C.; De Groot, F. M. F.; Tolentino, H. C. N.; Ramos, A. Y.; Massa, N. E.; Alonso, J. A.; Martínez-Lope, M. J. Spin-Orbit-Induced Mixed-Spin Ground State in $RNiO_3$ Perovskites Probed by X-Ray Absorption Spectroscopy: Insight into the Metal-to-Insulator Transition. *Phys. Rev. B: Condens. Matter Mater. Phys.* **2005**, *71*, 020406.
(42) Meyers, D.; Liu, J.; Freeland, J. W.; Middey, S.; Kareev, M.; Kwon, J.; Zuo, J. M.; Chuang, Y. De; Kim, J. W.; Ryan, P. J.;

https://dx.doi.org/10.1021/acs.nanolett.0c04538
Nano Lett. 2021, 21, 2436−2443

Chakhalian, J. Pure Electronic Metal-Insulator Transition at the Interface of Complex Oxides. *Sci. Rep.* **2016**, *6*, 27934.
(43) Kavich, J. J.; Warusawithana, M. P.; Freeland, J. W.; Ryan, P.; Zhai, X.; Kodama, R. H.; Eckstein, J. N. Nanoscale Suppression of Magnetization at Atomically Assembled Manganite Interfaces: XMCD and XRMS Measurements. *Phys. Rev. B: Condens. Matter Mater. Phys.* **2007**, *76* (1), 1−8.
(44) Catalano, S.; Gibert, M.; Bisogni, V.; He, F.; Sutarto, R.; Viret, M.; Zubko, P.; Scherwitzl, R.; Sawatzky, G. A.; Schmitt, T.; Triscone, J.-M. Tailoring the Electronic Transitions of $NdNiO_3$ Films through $(111)_{pc}$ Oriented Interfaces. *APL Mater.* **2015**, *3* (6), 062506.
(45) Domínguez, C.; Georgescu, A. B.; Mundet, B.; Zhang, Y.; Fowlie, J.; Mercy, A.; Waelchli, A.; Catalano, S.; Alexander, D. T. L.; Ghosez, P.; Georges, A.; Millis, A. J.; Gibert, M.; Triscone, J. M. Length Scales of Interfacial Coupling between Metal and Insulator Phases in Oxides. *Nat. Mater.* **2020**, *19*, 1182−1187.
(46) Abbate, M.; Zampieri, G.; Prado, F.; Caneiro, A.; Gonzalez-Calbet, J. M.; Vallet-Regi, M. Electronic Structure and Metal-Insulator Transition in $LaNiO_{3-\delta}$. *Phys. Rev. B: Condens. Matter Mater. Phys.* **2002**, *65* (15), 1−6.
(47) Suntivich, J.; Hong, W. T.; Lee, Y. L.; Rondinelli, J. M.; Yang, W.; Goodenough, J. B.; Dabrowski, B.; Freeland, J. W.; Shao-Horn, Y. Estimating Hybridization of Transition Metal and Oxygen States in Perovskites from O K-Edge X-Ray Absorption Spectroscopy. *J. Phys. Chem. C* **2014**, *118* (4), 1856−1863.
(48) Kang, J. S.; Lee, S. S.; Kim, G.; Lee, H. J.; Song, H. K.; Shin, Y. J.; Han, S. W.; Hwang, C.; Jung, M. C.; Shin, H. J.; Kim, B. H.; Kwon, S. K.; Min, B. I. Valence and Spin States in Delafossite $AgNiO_2$ and the Frustrated Jahn-Teller System $ANiO_2$ (A = Li,Na). *Phys. Rev. B: Condens. Matter Mater. Phys.* **2007**, *76*, 195122.
(49) Medarde, M.; Fontaine, A.; García-Muñoz, J. L.; Rodríguez-Carvajal, J.; De Santis, M.; Sacchi, M.; Rossi, G.; Lacorre, P. $RNiO_3$ Perovskites (R = Pr,Nd): Nickel Valence and the Metal-Insulator Transition Investigated by X-Ray-Absorption Spectroscopy. *Phys. Rev. B: Condens. Matter Mater. Phys.* **1992**, *46*, 14975.
(50) Middey, S.; Rivero, P.; Meyers, D.; Kareev, M.; Liu, X.; Cao, Y.; Freeland, J. W.; Barraza-Lopez, S.; Chakhalian, J. Polarity Compensation in Ultra-Thin Films of Complex Oxides: The Case of a Perovskite Nickelate. *Sci. Rep.* **2015**, *4*, 1−7.
(51) Cueva, P.; Hovden, R.; Mundy, J. A.; Xin, H. L.; Muller, D. A. Data Processing for Atomic Resolution Electron Energy Loss Spectroscopy. *Microsc. Microanal.* **2012**, *18* (4), 667−675.
(52) Lichtert, S.; Verbeeck, J. Statistical Consequences of Applying a PCA Noise Filter on EELS Spectrum Images. *Ultramicroscopy* **2013**, *125*, 35−42.
(53) Maigné, A.; Wolf, M. Low-Dose Electron Energy-Loss Spectroscopy Using Electron Counting Direct Detectors. *Microscopy* **2018**, *67* (suppl_1), i86−i97.
(54) Cheng, S.; Pofelski, A.; Longo, P.; Twesten, R. D.; Zhu, Y.; Botton, G. A. The Performance Evaluation of Direct Detection Electron Energy-Loss Spectroscopy at 200 KV and 80 KV Accelerating Voltages. *Ultramicroscopy* **2020**, *212*, 112942.

https://dx.doi.org/10.1021/acs.nanolett.0c04538
Nano Lett. 2021, 21, 2436−2443